

# Modeling and Analysis of Delay Doppler Maps for Spaceborne GNSS-R Signal Scattered from Sea Surface

Min Chen<sup>1</sup>, Peng-Ju Yang<sup>1,2,\*</sup>, and Rui Wu<sup>1</sup>

<sup>1</sup>*School of Physics and Electronic Information, Yan'an University, Yan'an 716000, China*

<sup>2</sup>*Key Laboratory for Information Science of Electromagnetic Waves (MoE), Fudan University, Shanghai 200433, China*

**ABSTRACT:** The Global Navigation Satellite System Reflected (GNSS-R) Signal adopts a heterogeneous observation mode and utilizes the globally shared GNSS constellation as a multisource microwave signal transmission source, providing the opportunity signals for radar measurements. As a basis for GNSS-R bistatic remote sensing simulations, this paper analyzes wave spectrum model of sea surfaces, GNSS signal scattering model, and GNSS signal scattering power model. The modified Zavorotny and Voronovich (Z-V) model combined with two-scale method (TSM) for sea surface scattering is utilized to simulate the delay Doppler map (DDM), with emphasis on the analysis of the effects of wave polarizations, delay Doppler interval, and sea states on DDM of GNSS signal scattered from sea surfaces. The correlated power model of GNSS scattering signal is validated by comparison with measured Cyclone Global Navigation Satellite System (CYGNSS) DDM data in L1 level 2.1 version. The DDM waveforms obtained from Z-V model combined with TSM are basically consistent with the CYGNSS actual data, in which strong scattering spots can be observed clearly from both simulated and measured DDMs. The modeling and analysis of DDM for spaceborne GNSS-R signal from sea surface is of great value in ocean remote sensing applications, particularly for the interpolation and utilization of various spaceborne GNSS measured data.

## 1. INTRODUCTION

Storm surges, heavy rainfall, and destructive storms caused by tropical cyclones pose a significant threat to the safety of marine equipment and coastal areas around the world. In the process of studying tropical cyclones, remote sensing satellites utilize non-contact methods to detect and acquire surface physical parameters, such as global land and ocean characteristics [1]. This approach offers extensive observation coverage and a wide imaging range. In 1935, Robert Watson-Watt conducted the “Davenport Experiment”, which marked the inaugural validation experiment to detect targets in flight status using external radiation sources in short-distance scenarios. This milestone initiated research into external radiation sources as opportunistic sources of illumination [2]. Among them, global navigation satellite systems reflectometry (GNSS-R) remote sensing technology [3, 4] is a crucial component of ocean remote sensing technology. This technology can furnish crucial monitoring data for various fields, including sea surface wind speed, sea ice detection [5, 6], soil moisture detection [7–9], and water distribution detection [10, 11]. Moreover, it offers remote sensing signal sources for different topological structures.

In 2003, the British National Space Centre launched the GNSS-R receiver on the UK-DMC-1 satellite. This satellite marked the first successful collection of delay Doppler map (DDM) data from spaceborne earth observation satellites. It is a disaster monitoring constellation spanning multiple countries, with the capability to collect data from 40 specular reflection points on the ocean’s surface [12–14]. In 2014, the

Surrey Satellite Company in the UK launched a new onboard GNSS receiver into orbit on TDS-1, which can obtain DDM measurement images and extract sea surface wind speed information [15, 16]. Following the UK TDS-1 mission, the international space station GEROS-ISS mission was proposed to utilize the L-band of GNSS-R signals to determine physical parameters associated with climate characteristics, such as sea surface height and root mean square slope. The mission encompassed various output parameters, thereby verifying the feasibility of GNSS-R land remote sensing applications [17, 18]. In 2016, NASA launched cyclone global navigation satellite system (CYGNSS), which leveraged the insensitivity and strong penetration of GNSS-R in the L-band on the earth’s surface to obtain real-time wind speed information at different locations during storm conditions. The primary objectives of the CYGNSS mission were initially to study and monitor the intensity and rainfall of tropical cyclones [19–21]. In 2017, Japan’s Weathernews company launched the WNISAT-1R satellite, which receives GNSS signals and generates DDM [22]. In 2022, NASA launched the TROPICS cube satellite constellation, with emphasis on the sampling of tropical cyclones and monitoring of characteristic parameters within storms [23].

Research on related GNSS-R tasks is gradually commencing in China as well. In 2019, China launched BuFeng-1 A/B twin satellites. This mission marked a significant advancement in detecting wind field data information across various sea areas and represented China’s inaugural engineering practice in the field of GNSS-R [24]. In 2020, the establishment of China’s self-developed Beidou navigation satellite system

\* Corresponding author: Pengju Yang (pjyang@fudan.edu.cn).

(BDS) has provided navigation positioning and timing services for global users. This development holds significant importance for China's advancements in the field of satellite navigation, while also presenting another reliable satellite navigation option for worldwide users [25]. In 2021, Tianjin University independently developed and launched Jilin-1 Wide Range 01B satellite, marking the first commercial satellite in China equipped with reflection detection payloads. This satellite enables the acquisition of ocean wind field data information around the clock. In 2023, China launched the Remote Sensing 36 satellite, designed to provide climate and environmental information pertinent to global change.

Currently, in the field of GNSS-R signal modeling and delay Doppler power spectrum simulation, research teams have made significant progress [26–28]. They have developed relevant simulation tools and conducted corresponding research based on these tools. For instance, CYGNSS E2ES simulation software [29], GREEPS simulation software [30], and SAVERS simulation software [31] are among the notable examples. These simulators facilitate the simulation and analysis of the delay Doppler effect and signal power distribution in wireless communication. The comprehensive simulation of the entire link holds great significance for studying delay Doppler characteristics.

The research on delay Doppler imaging requires practical applications for further expansion and fusion. Melebari et al. have improved the existing GNSS-R DDM model by incorporating shortwave diffraction due to small-scale ground roughness and signal attenuation caused by vegetation. The peak reflectance and DDM shape were investigated using the DDMs of the CYGNSS mission. The aforementioned study illustrates that the model effectively predicts the CYGNSS DDMs at these two validation points [32]. Nabi et al. employed a deep learning framework to estimate surface humidity values using CYGNSS-measured data, thus showcasing the viability of utilizing DDM for retrieving the deep learning domain and estimating physical feature parameters under diverse surface and resolution conditions [33]. Although there is currently more research on the application of CYGNSS measured data in various countries, the study of navigation satellite signals still requires a large amount of experimental foundation. Furthermore, the repeatability of experiments is compromised by the influence of climate and sea conditions, necessitating stricter testing scenario requirements. Therefore, the modeling of theoretical models also provides a foundation and guarantee for the analysis of indicators and system optimization of launching satellites. In this article, the geometric model employs a bistatic radar configuration and extracts relevant physical characteristics of the reflecting surface by utilizing the reflected navigation satellite pseudo-random ranging code signal or carrier signal. The changes in waveform, polarization characteristics, and associated parameters directly mirror the attributes of the reflecting surface, with the goal of obtaining more information about target parameters. Concurrently, the considerations encompass the equivalent isotropic radiated power (EIRP) and comprehensive coverage characteristics. Building upon the principles of ocean remote sensing technology, the GNSS constellation serves as a multisource microwave external radiation source.

Valuable information on sea conditions, such as wind speed and direction, is obtained by discerning the relevant power distribution of ocean surface signals and sea surface roughness through both direct and reflected signals. This satellite remote sensing approach leverages scattering effects. Simulation of DDM is conducted, with the resulting simulations compared and analyzed against actual power spectra extracted from CYGNSS data to validate the feasibility of the simulation. Additionally, future prospects for the field of ocean remote sensing are also discussed.

This paper is organized as follows. Section 2 introduces each version of CYGNSS data and clarifies basic parameters and related characteristics. In Section 3, principles of GNSS-R bistatic remote sensing are presented, and the theoretical simulations are described and analyzed. In Sections 4, this section analyzes wave spectrum model of sea surfaces, GNSS signal scattering model, and GNSS signal scattering power model. In Sections 5, simulation results and discussion are presented, and some factors that affect DDM imaging are analyzed. At the same time, the simulation results are compared and analyzed with the measured data of CYGNSS. Finally, Section 6 concludes this paper.

## 2. CYGNSS SATELLITE REMOTE SENSING DATA

### 2.1. CYGNSS Data

The CYGNSS satellite was launched by NASA on December 15, 2016, and it has been providing free observation data since March 2017. It comprises eight constellation satellites positioned in low earth orbit observation stations, and each satellite comprises four reflection channels. Each satellite maintains an orbital inclination of 35 degrees and operates at an altitude of 510 km. The observation area covers a strip of 40 degrees north-south latitude, with a full coverage of east-west longitude [34]. This specific orbital design enables the satellite to capture tropical cyclones from multiple angles, thereby enhancing the comprehensiveness of the data collected.

The entire spatial geometry system adopts a bistatic topology structure with separate transmission and reception capabilities. The GNSS satellite constellation functions as the launch station, while the delay Doppler imaging instrument (DDMI) integrated into the CYGNSS receiving station is utilized for receiving both direct signals and signals reflected from the ocean surface [35]. The signals are measured at a frequency of 1 Hz, and the DDMI has the capacity to concurrently capture and process four GPS signals. Each reflected signal yields one DDM per second, resulting in a maximum of 86400 DDM images provided daily. These images are sampled at intervals of 0.25 chips and 500 Hz, with a maximum of 32 simultaneous measurements per second achievable. Additionally, the average revisit time for the CYGNSS satellite constellation is approximately 2.8 hours, ensuring frequent and comprehensive coverage of the observation area. To enhance data transmission rates, CYGNSS compresses the original DDMs with practical measures. The practical measured DDM corresponds to a delay resolution of approximately 0.25  $\mu$ s, a length resolution about 74 m, and a spatial resolution that needs to be determined over an area of 25 km  $\times$  25 km. The

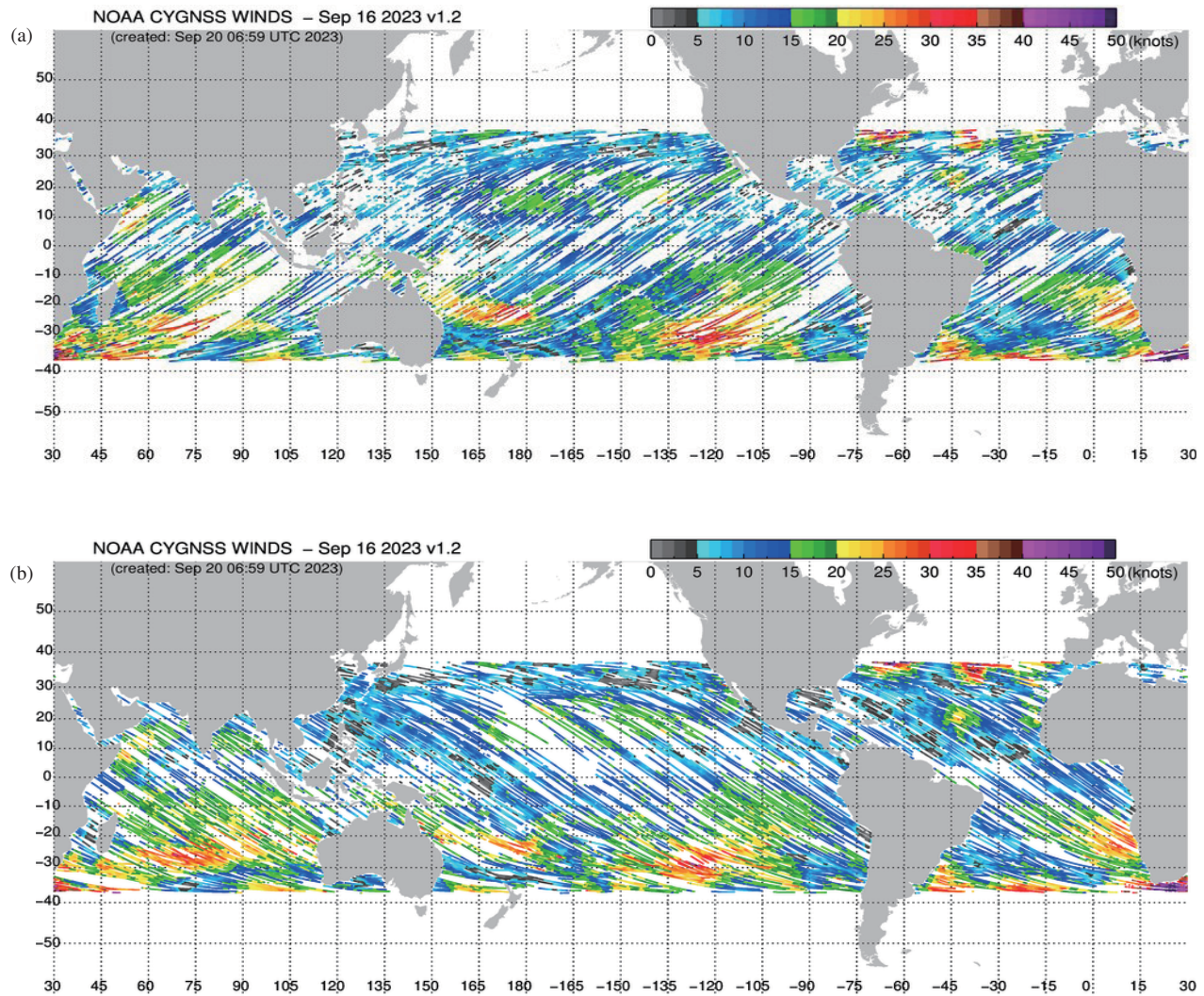


FIGURE 1. CYGNSS observations of global wind field images.

DDM obtained by CYGNSS represents the relevant power extracted from the signal through selective filtering based on delay and Doppler characteristics. The delay refers to the difference in arrival time between a direct signal and a scattered signal at the receiver, while the Doppler frequency shift is caused by the relative motion of the transmitter and receiver, as well as the relative motion of the reflector.

This article utilizes data from the CYGNSS L1 level 2.1 version Cyg04 satellite in orbit. The CYGNSS metadata encompasses delay Doppler sample data along with a series of related measurement and navigation information parameters. These parameters primarily include the delay Doppler map of normalized bistatic radar cross sections (NBRCS), the delay Doppler map average (DDMA) near specular reflection points, and the corresponding metadata of the leading edge slope (LES) of delay waveforms. The CYGNSS data undergoes compression to generate a netCDF file format. Each data file contains satellite data for a 24-hour period in coordinated universal time (UTC). An example image of the daily NOAA CYGNSS global wind is shown in Fig. 1, with each image containing global wind data from the CYGNSS observation station [36]. Fig. 1 shows the

TABLE 1. Parameters and characteristics of CYGNSS.

Parameter	Characteristic
Operating Frequency	1575.42 MHz
Spatial Resolution	Approximately 25 square kilometers
Orbital Information	The inclination angle of the track is

observed data on September 16, 2023. The basic parameters and related characteristics of CYGNSS are shown in Table 1.

## 2.2. CYGNSS Raw Intermediate Frequency Data

The current publicly available raw data of the CYGNSS satellite includes intermediate frequency (IF) data containing phase information. Each CYGNSS raw intermediate frequency data is acquired by the receiving station and is subsequently processed on the ground. The CYGNSS raw dataset comprises a raw IF data file accompanied by its corresponding metadata

file. Each raw IF data stream encompasses three sets of raw sample streams, which undergo amplification and conversion to baseband at the RF frontend. The input RF streams from three distinct antenna channels are then digitized for further processing. The raw intermediate frequency data of CYGNSS is collected by sensors, typically spanning a duration of 30 to 90 seconds, commonly set at 60 seconds, to construct higher resolution DDM data. Table 2 presents the basic parameters and related characteristics of CYGNSS raw intermediate frequency data.

**TABLE 2.** Parameters and characteristics of CYGNSS IF.

Parameter	Characteristic
Operating Frequency	1575.42 MHz
Center Frequency	3.8724 MHz
Sampling Frequency	13.0362 MHz
Bandwidth	2.5 MHz
Coverage	[−45, 45]

### 3. PRINCIPLES OF GNSS-R BISTATIC REMOTE SENSING

#### 3.1. GNSS-R Geometric Model

##### 3.1.1. Macro-Geometric Relationships

This article adopts a bistatic configuration with separate transmission and reception. This heterologous observation mode improves spatiotemporal resolution by using noncontact methods. The precise construction of GNSS-R spatial geometric models is essential for investigating ocean remote sensing theory and conducting simulation analyses. This article employs a scattering reference frame (SRF) with a specular reflection point (SP) serving as the coordinate origin. This spatial geometric elucidates the spatial geometric relationships among GNSS satellites, low orbit satellites, and specular reflection points at a macroscopic level. The incident wave can be treated as a parallel beam of light due to the high altitude of GNSS satellites above the earth’s surface. The geometric configuration of GNSS-R is illustrated in Fig. 2.

As illustrated in Fig. 2, low earth orbit satellites not only receive direct signals, but also signals reflected from the earth’s surface. Among them,  $\vec{v}_r = (v_{rx}, v_{ry}, v_{rz})$  and  $\vec{v}_t = (v_{tx}, v_{ty}, v_{tz})$  are the velocities of low Earth orbit satellites and GNSS satellites, respectively.  $\alpha_r$  and  $\alpha_t$  represent the angles between low earth orbit satellite and GNSS satellite and the  $x$ -axis.  $\theta$  is the altitude angle of GNSS satellites, and  $R_e$  is the radius of the earth. In the modeling of spaceborne scenes, it is imperative to account for the curvature of the earth to precisely calculate the visible range of the antenna and the coverage area of the glistening zone. Hence, the radius of the earth was determined using the world geodetic system 1984 (WGS-84) earth ellipsoid model. The positions of receivers aboard GNSS satellites, low orbit satellites, and any points on the earth’s surface

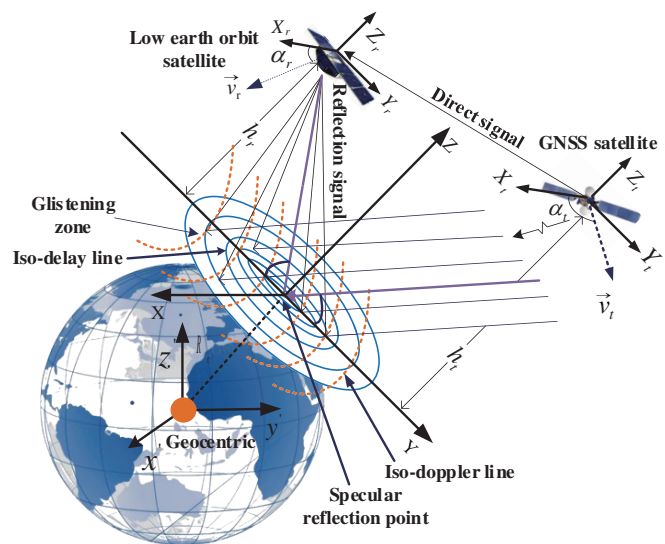


**FIGURE 2.** GNSS-R macro-geometric relationships.

can be accurately represented accordingly.

$$R_t = \left( 0, \frac{h_t}{\tan \theta}, h_t \right) \quad (1)$$

$$R_r = \left( 0, \frac{h_r}{\tan \theta}, h_r \right) \quad (2)$$

$$\rho = (x, y, z) \quad (3)$$

In the above formula,  $h_t$  and  $h_r$  express GNSS satellite and low orbit satellite orbit heights, respectively.

##### 3.1.2. GNSS-R Micro-Geometric Relationship

The micro-geometric relationship of GNSS-R, denoting the scattering interactions of individual reflection units within the scattering region, is depicted in Fig. 3.

The scattering field observed by the GNSS-R receiver at the grid scattering point, characterized by polarization angle  $\theta_i$  and

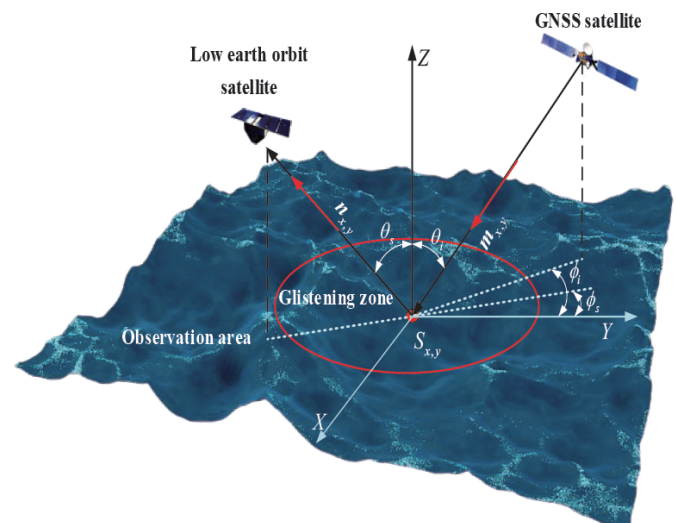


**FIGURE 3.** GNSS-R micro-geometric relationships.

azimuth angle  $\phi_i$ , can be expressed as follows.

$$\vec{m}_{x,y} = k(\hat{x} \sin \theta_i \cos \phi_i + \hat{y} \sin \theta_i \sin \phi_i - \hat{z} \cos \theta_i) \quad (4)$$

$$\vec{n}_{x,y} = k(\hat{x} \sin \theta_s \cos \phi_s + \hat{y} \sin \theta_s \sin \phi_s - \hat{z} \cos \theta_s) \quad (5)$$

$$S_{x,y} = k(\vec{n}_{x,y} - \vec{m}_{x,y}) = (q_{\perp}, q_z) \quad (6)$$

In the above formula,  $\vec{m}_{x,y}$  represents the incident signal vector, and  $\vec{n}_{x,y}$  represents the scattered signal vector.  $k$  represents the number of electromagnetic signal waves. The scattering vector of scattering unit  $S_{x,y}$  is represented as follows. In Eq. (6),  $q_{\perp}$  and  $q_z$  represent the horizontal and vertical components of the scattering signal vector, respectively. When electromagnetic waves produce mirror reflection,  $\theta_i$  and  $\theta_s$  correspond equally to  $\phi_i$  and  $\phi_s$ .

### 3.2. GNSS Signal Structure and DDM Mapping

This article employs GPS L1 C/A signal as an example to investigate GNSS-R imaging. GNSS signal can be conceptualized as a quasi-monochromatic phase-modulated spherical wave signal, with the GPS signal being a modulated signal. Hence, the direct signal and reflected signal emitted by the  $i$ -th GPS satellite can be formulated as follows.

$$S_d(t) = A_i D_i(t - \Delta\tau_d) B_i(t - \Delta\tau_d) \cdot \cos[2\pi f_{L1}(t - \Delta\tau_d) + \theta_i] \quad (7)$$

$$S_r(t) = \sum_{i=1}^n A_i D_i(t - \Delta\tau_i) B_i(t - \Delta\tau_i) \cdot \exp[-j2\pi f_i(t - \Delta\tau_i) + \theta_i] \quad (8)$$

In Eqs. (7) and (8),  $A_i$  is the signal amplitude, and  $B_i(t)$  is the pseudo-random code sequence.  $D_i(t)$  is the navigation message from GPS satellites.  $f_{L1}$  is the frequency of the carrier signal.  $\theta_i$  is the initial signal phase of the carrier caused by frequency drift and phase noise.  $\Delta\tau_d$  is the delay of GNSS direct signal. In Eq. (8),  $\Delta\tau_i$  and  $f_i$  represent signal delay and Doppler frequency shift of GNSS reflection signals, respectively. Navigation information may induce phase jumps and affect the signal-to-noise ratio of the outcomes. Consequently, the impact of data codes is often disregarded in practical analysis. The spectrum distribution of C/A code, P code, and their synthesized signals and the C/A ambiguity function are shown in Fig. 4 and Fig. 5. The ambiguity function (AF) can comprehensively reveal the internal structural information of signals, thereby uncovering effective features that differentiate them from other signals.

Fig. 4 illustrates that the delay and frequency of the sea surface reflection signal can be precisely mapped, constituting known information. Accurate modeling of GNSS-R ocean remote sensing is imperative for extracting one-dimensional and two-dimensional measured medium features and for conducting correlated power two-dimensional imaging. The geometric model delineates the spatial system of GNSS-R signals, elucidating the relative and absolute geometric position relationships among the transmitter, specular reflection point, and receiver. The precise construction of both macroscopic and microscopic GNSS-R spatial geometric models serves as the bedrock for

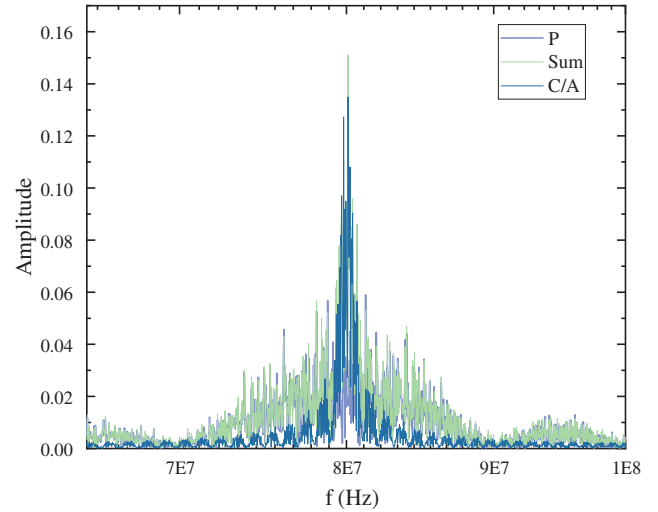


FIGURE 4. GPS signal spectrum.

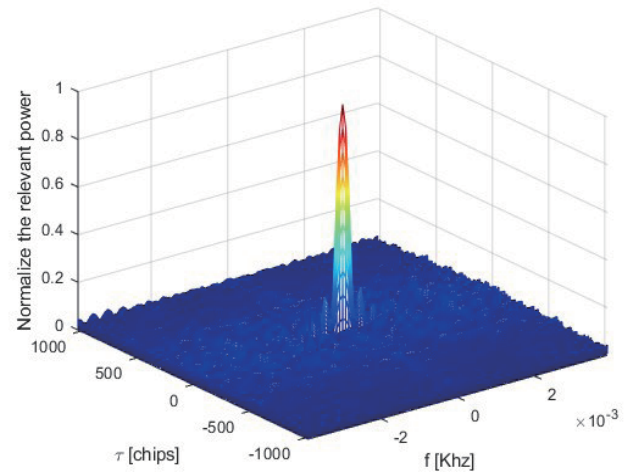


FIGURE 5. C/A ambiguity function.

subsequent imaging endeavors. GNSS reflected signals generally show the attenuation of signal amplitude due to propagation characteristics and sea surface roughness.

### 3.3. Cross-Correlation Function of Reflected Signal

Due to the low power of GNSS reflection signals, direct power measurement and analysis are unfeasible. Therefore, it is essential to employ relevant processing techniques to amplify the signal and ensure its adequacy for subsequent analysis. At any given time, the correlation function between the pseudo-random code copy of the GNSS reflection signal and the signal output by the receiving antenna can be expressed as the correlation value between the received reflection signal and local signal.

$$Y(t_0, \tau, f_c) = \int_0^{T_i} a(t_0 + t') u(t_0 + t' + \tau) e^{-j2\pi t' f_c} dt' \quad (9)$$

$$\Lambda[\delta\tau(\rho)] = \frac{1}{T_i} \int_0^{T_i} a(t_0 + t') a[t_0 + t' + \delta\tau(\rho)] dt' \quad (10)$$

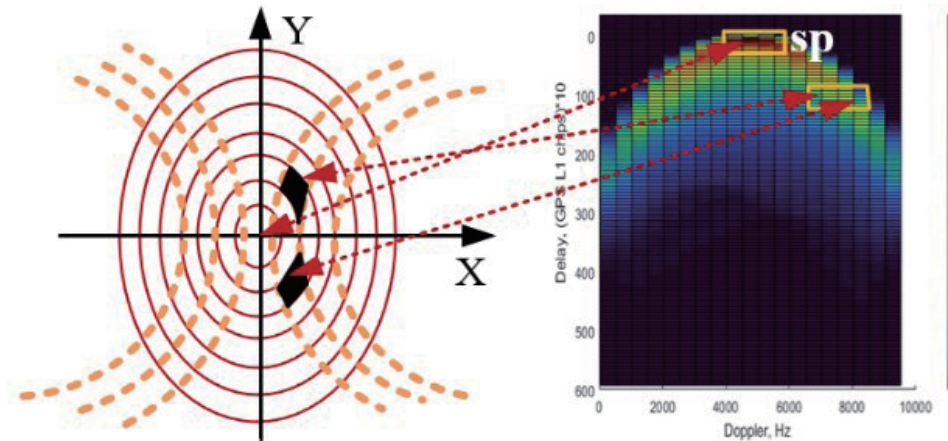


FIGURE 6. Mapping relation of reflective surface cells to delay doppler power maps.

$$\begin{aligned} \text{sinc}[\delta f(\rho)] &= \frac{1}{T_i} \int_0^{T_i} \exp[-2\pi j \delta f(\rho) t'] dt' \\ &= \frac{\sin[\pi \delta f(\rho) T_i]}{\pi \delta f(\rho) T_i} \exp[-\pi j \delta f(\rho) T_i] \end{aligned} \quad (11)$$

After simplification calculation, the cross-correlation function of GNSS reflection signal is obtained as follows.

$$\begin{aligned} Y(t_0, \tau, f_c) &= AT_i \exp(2\pi j f_c t_0) \\ &\cdot \iint D_\rho(\rho) \Lambda[\delta \tau(\rho)] \text{sinc}[\delta f(\rho)] g(\rho, t_0 + \tau) d^2 \rho \end{aligned} \quad (12)$$

In Eq. (12),  $T_i$  represents the integration time, and  $f_c$  is used to compensate for the Doppler frequency shift of the received signal.

### 3.4. Correlated Power of Reflected Signal

DDM is a function of signal delay and Doppler frequency shift from specular reflection points. The correlated power of the reflection signal after incoherent accumulation, representing the delay and Doppler characteristics of the reflection surface unit relative to the specular reflection point, can be expressed as follows.

$$\begin{aligned} \tau_{xy} &= \sqrt{x^2 + \left(y + \frac{h_r}{\tan \theta}\right)^2 + (h_r - z)^2} \\ &\quad - \frac{h_r}{\sin \theta} - y \cos \theta - z \sin \theta \end{aligned} \quad (13)$$

$$\begin{aligned} f_d &= v_t \cdot R_t - v_r \cdot R_r = -v_{ty} \cdot \cos \theta - v_{tz} \cdot \sin \theta \\ &\quad + \frac{v_{rx} \cdot x + v_{ry} \cdot \left(y + \frac{h_r}{\tan \theta}\right) - v_{rz} \cdot z - h_r}{\sqrt{x^2 + \left(y + \frac{h_r}{\tan \theta}\right)^2 + (h_r - z)^2}} \end{aligned} \quad (14)$$

In the above formula,  $z = \sqrt{R_e^2 - x^2 - y^2} - R_e$ .  $\tau_{xy}$  is a delay increment.  $f_d$  is the Doppler frequency offset. Indeed,

GNSS reflection signals exhibit complex signal characteristics with the mapping relationship between the spatial domain and the delay Doppler domain serving as the core aspect in exploring DDM imaging. The mapping relationship between the reflector unit and delay Doppler power spectrum is depicted in Fig. 6.

As illustrated in Fig. 6, SP represents a specular reflection point. In the mapping relationship between the spatial domain and delay Doppler domain, not every reflector unit uniquely corresponds to a delay Doppler region. There exist two intersections between the iso-delay line and iso-Doppler line in the spatial domain. Consequently, the iso-delay loops and adjacent iso-Doppler bands delineate two distinct reflector units in space. When two different reflector units are mapped into the same delay Doppler region, the reflection signals from each reflector unit overlap or are superimposed, resulting in the formation of the GNSS reflection signal [35]. Hence, DDM serves not only to illustrate the distribution of GNSS-R signals in the delay Doppler domain but also to indicate the intensity of scattering power in the spatial domain. In general, the intersection of iso-delay lines and iso-Doppler lines results in the formation of a tilted grid unit, which is represented as the contour of the Woodward ambiguity function (WAF) in bistatic radar. The reflection intensity of the reflection surface unit can be effectively described by processing the different colors and amplitudes of the generated DDM. This allows for the accurate optimization of reflection characteristics across the time-frequency domain and facilitates the segmentation of the sea surface scattering area.

Conducting correlation operations enables the capture of different Doppler bands at various center frequencies, each corresponding to distinct delay waveforms in DDM. As the distance from the specular reflection point increases, the power of the one-dimensional delay waveform diminishes, and the corresponding peak value of the waveform is also delayed. The size of the reflection footprint on the DDMs increases with the roughness of the reflective surface. This phenomenon can be illustrated in Fig. 7.

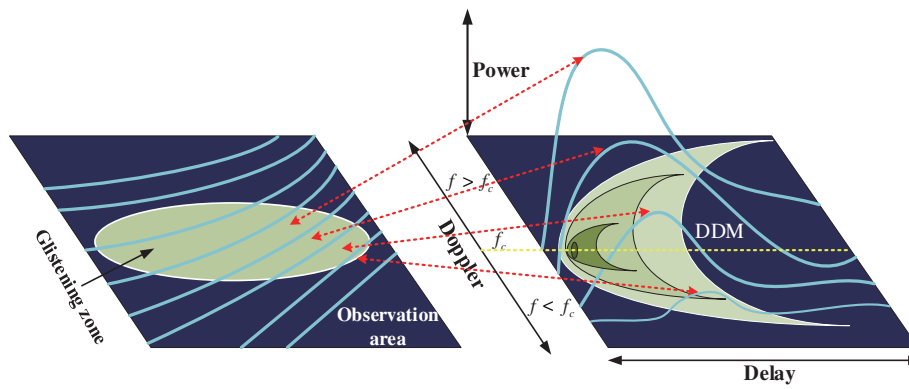


FIGURE 7. Visual representations of reflection waveforms in a DDM.

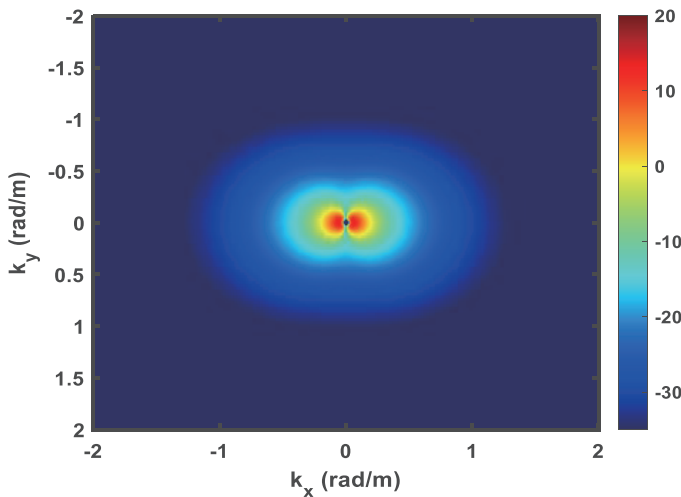


FIGURE 8. Visual representations of reflection waveforms in a DDM.

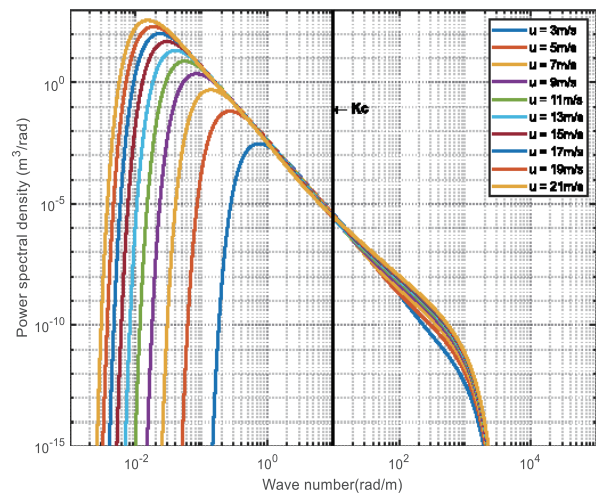


FIGURE 9. Elfouhaily wave spectrum.

## 4. POWER MODEL OF OCEAN-SCATTERED GNSS SIGNALS

### 4.1. Wave Spectrum Model

Ocean waves can be regarded as a combination of various amplitude, frequency, direction, and phase, and have complex characteristics. The Elfouhaily wave spectrum [36] is a commonly utilized two-dimensional wave spectrum in sea surface remote sensing inversion applications, and it comprises two components: radial and azimuthal. At the same time, the model considers the impact of wind drive on energy, which can be represented as follows.

$$S(k, \varphi) = M_E(k)Y(k, \varphi) \quad (15)$$

$$M_E(k) = k^{-3}[B_l(k) + B_h(k)]L(k)\Gamma^{\gamma(k)} \quad (16)$$

$$Y(k, \varphi) = \frac{1}{2\pi}(1 + \Delta(k, U_{10}) \cos(2\varphi)) \quad (17)$$

In the formula,  $M_E(k)$  represents the radial component of the wave spectrum, and  $Y(k, \varphi)$  denotes the azimuth function corresponding to the wave spectrum.  $k$  is the wavenumber.  $\varphi$  signifies the wave direction, while  $B_l$  and  $B_h$  represent the low-frequency and high-frequency components of the wave spectrum, respectively. The corresponding orientation function is

illustrated in Fig. 8. The larger the wave number of Elfouhaily waves is, the gradually decreasing the value of power spectral density is. As the wind speed increases, the spectral peak shifts towards lower frequencies. By combining the frequency spectrum with random phase and using inverse Fourier transform, the fluctuations in the frequency domain are transformed into the sea surface height field in the spatiotemporal domain.

The Elfouhaily wave spectrum consists of both high and low frequencies. Consequently, the power spectral density of the Elfouhaily wave spectrum fluctuates with the shape of the wavenumber under various wind speed conditions based on the above expression, as depicted in Fig. 9. As illustrated in Fig. 9,  $k_c$  represents the cutoff wavenumber of the sea spectrum. Given that the  $k_c$  of the GPS L1 signal is approximately 10 rad/m, the power spectral density in the right half of Fig. 9 corresponds to the large-scale roughness of sea surface, while the left half depicts small-scale roughness.  $k_c$  illustrates large-scale roughness, while the left half depicts small-scale roughness. As wind speed escalates, the spectral peak shifts towards the low-frequency direction, and it results in an augmentation of total energy in wind and waves. Consequently, the scattering coefficient diminishes and leads to enhanced diffuse reflection.

The mean square slope (MSS) serves as a physical parameter utilized to quantify the variation in slope of sea waves and the

roughness of the sea surface [37]. It can be derived from the Elfouhaily wave spectrum model and is expressed as follows.

$$MSS = \int_0^{k^*} \int_{-\pi}^{\pi} k^2 S(k, \varphi) d\varphi dk \quad (18)$$

The larger the wave number of Elfouhaily waves is, the gradually decreasing the value of power spectral density is. As the wind speed increases, the spectral peaks shift towards lower frequencies. By combining the spectrum with random phases and using inverse Fourier transform, the fluctuations in the frequency domain are transformed into a sea surface height field in the spatiotemporal domain. The random sea surface generated based on the Elfouhaily sea spectrum model is shown in Fig. 10.

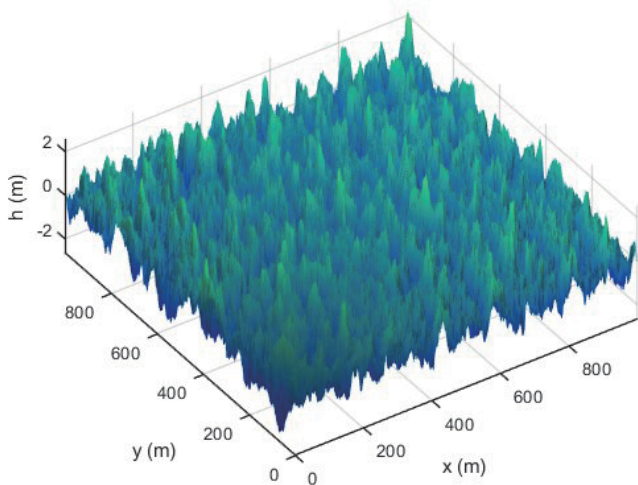


**FIGURE 10.** Random sea surface based on Elfouhaily’s sea spectral model.

#### 4.2. Electromagnetic Scattering Model for Sea Surfaces

In traditional GNSS-R simulation processes, the Kirchhoff approximation-geometric optics (KA-GO) model is commonly employed [38]. The model predominantly computes the scattered field at a point on a relatively flat rough surface by utilizing the scattered field acquired through specular reflection on an infinite tangent plane at that point. It primarily employs the concept of tangent plane approximation. Nevertheless, the tangent plane approximation method overlooks the effects caused by scattering. This property limit its applicability in practical calculations. The two scale electromagnetic scattering method treats the sea surface as a composite surface comprising two different sizes. This approach enables small-scale scattering contributions to be modulated by large-scale modulation, thereby capturing the overall rough surface scattering characteristics. The two scale electromagnetic scattering method combines elements of both the KA-GO and the small perturbation method (SPM). This approach is versatile, allowing for the measurement of rough sea surfaces spanning both large and small scales. Therefore, this article uses the two scale electromagnetic scattering method to simulate GNSS-R on the basis of traditional models.

Under the KA-GO approximation, the normalized birefringent radar cross section of seawater can be expressed as [39]

$$\sigma_0 = \frac{\pi |\Re|^2 q^4}{q_z^4} P_{pdf} \left( -\frac{q_{\perp}}{q_z} \right) \quad (19)$$

In the formula,  $\Re$  represents the fresnel reflection coefficient of the signal on the sea surface. When the MSS falls within a certain range denoted by  $P_{pdf}$ , this probability density function can be employed to compute the dynamic and statistical characteristics of the sea surface reflection signal and utilize a wave spectrum model for calculation.  $q$  is a vector utilized to describe the reflection geometry relationship between GNSS satellites, reflector elements, and low orbit satellites.  $q$ ,  $q_{\perp}$ , and  $q_z$  represent the mode of the scattering vector  $q$ , the horizontal component of  $q$ , and the mode of the normal component, respectively.

When an incident electromagnetic wave interacts with a rough surface, the rough surface will generate plane wave components with varying amplitudes by specific scattering mechanisms under SPM conditions. The scattering outcomes of the perturbation method can be derived by superimposing various plane wave components. Consequently, the normalized bistatic radar scattering cross-section of seawater can be expressed as follows.

$$\begin{aligned} \sigma_{spm} &= 4\pi k_1^2 \cos^2 \theta_2 f(k_{1x}, k_{1y}) \\ &= 8|k_1^2 \delta \cos \theta_1 \cos \theta_2 \Re_{pq}|^2 W(2k \sin \theta_1, \varphi_1; U_{10}, \varphi_{WD}) \end{aligned} \quad (20)$$

The two scale electromagnetic scattering method combines the KA-GO approximation method and SPM method, while considering the rough surface scattering results of different scales. Therefore, the representation of the two scale electromagnetic scattering method can be formulated as follows.

$$\sigma = \sigma_0 + \sigma_{spm} \quad (21)$$

The small angle curve from the KA-GO method is integrated with the medium and higher angle curve from the SPM to obtain a two scale curve. Viewed from this perspective, the two scale method amalgamates the benefits of both the KA-GO and SPM methods. In simulation, it is generally necessary to consider the influence of salinity and temperature of sea surface water on the reflection coefficient  $\Re$ , but the influence of these two factors can be ignored in GNSS-R simulation. Among these,  $P_{pdf}$  represents the pdf of sea surface slope and characterizes the distribution of mean square tilt of the sea surface. Assuming that the PDF follows a two-dimensional Gaussian distribution, it is computed using the Gram-Charlier distribution.

$$\begin{aligned} P_{pdf} &= \frac{1}{2\pi \sqrt{\sigma_u^2 \sigma_c^2}} \exp \left( -\frac{1}{2} \left( \frac{s_x^2}{\sigma_u^2} + \frac{s_y^2}{\sigma_c^2} \right) \right) \\ &\quad \left( 1 + \sum_{i,j} c_{ij} H_i \left( \frac{s_x}{\sqrt{\sigma_u^2}} \right) H_j \left( \frac{s_y}{\sqrt{\sigma_c^2}} \right) \right) \end{aligned} \quad (22)$$

$$\sigma_u^2 = 0.45 \times \{3.16 \times 10^{-3} f(U_{10}) \pm 0.004\} \quad (23)$$

$$\sigma_c^2 = 0.45 \times \{0.003 + 1.92 \times 10^{-3} f(U_{10}) \pm 0.002\} \quad (24)$$

$$f(U_{10}) = \begin{cases} U_{10} & U_{10} \leq 3.49 \\ 6 \cdot \ln(U_{10}) - 4 \cdot 3.49 & 3.49 < U_{10} \leq 46 \\ 0.411 \cdot U_{10} & U_{10} > 46 \end{cases} \quad (25)$$

In the formula,  $\sigma_u^2$  and  $\sigma_c^2$  are the mean square slope functions for headwinds and crosswinds, respectively.

### 4.3. Scattering Power Model

When the GNSS reflection signal interacts with a system comprising random sea surfaces, it can be approximated as the convolution of both and describe the effect of the signal on a linear time invariant system. In the bistatic configuration of GNSS-R, the acquired data from navigation satellite reflection signals are processed into DDM. Drawing upon microwave scattering theory, the bistatic radar equation for GNSS-R signals can be formulated using the Zavorotny and Voronovich (Z-V) model. This model considers factors such as propagation path, phase difference, signal polarization, and reflection coefficient post reflection, enabling the calculation of the power of GNSS-R signal following correlation with the locally generated pseudo-random code by the receiver. It can be represented as follows.

$$\langle |Y(\tau, f_d)|^2 \rangle = \frac{\lambda^2 T_i P_t G_t}{(4\pi)^3} \iint \frac{G_r}{R_t^2 R_r^2} \Lambda^2(\tau) \sin^2(f) \sigma d\rho \quad (26)$$

In the formula,  $\tau$  represents the time delay, and  $f_d$  is the Doppler frequency shift.  $T_i$  is the coherent integration time.  $\lambda$  is the signal carrier wavelength.  $P_t$  is the satellite launch power.  $G_t$  is the gain of the satellite launch antenna.  $G_r$  is the gain of the receiver antenna.  $R_t$  and  $R_r$  are the distances from the transmitter and receiver to the mirror reflection point, respectively.  $P_t G_t$  represents the effective omnidirectional radiation power of the navigation satellite. In the vicinity of the sea surface area near the mirror reflection point, the delay difference between the reflected signal and direct signal is minimal. Hence, the equivalent isotropic radiated power can be approximated as a constant.  $\Lambda(\tau)$  is the autocorrelation function of the pseudo-random code of the navigation satellite signal, and  $\sin^2(f)$  is the Doppler frequency shift function.  $\Lambda^2(\tau) \sin^2(f)$  is  $|\chi(\tau, f)|^2$ , which is the WAF function, mainly used to describe the coherent process of the reflected signal, and represents the selectivity of the correlated power on the Doppler frequency  $f$  and delay  $\tau$ .  $\sigma$  is the normalized birefringent radar scattering cross-section per unit area of the surface as a reflective surface. Due to the differences in specific situations of different reflective surfaces, the distribution of scattering coefficients per unit area varies.

To accelerate simulation speed, DDM in Eq. (27) can be represented in two-dimensional convolutional form.

$$\langle |Y(\tau, f_d)|^2 \rangle = \chi^2(\tau, f_d) * p_s(\tau, f_d) \quad (27)$$

$$5p_s(\tau, f_d) = \frac{T_i^2 P_t G_t \lambda^2}{(4\pi)^3}$$

$$\cdot \iint_G \frac{G_r \sigma_0(\rho)}{R_t^2 R_r^2} \delta[\tau - \tau(\rho)] \delta[f_d - f_d(\rho)] d^2\rho \quad (28)$$

In the formula,  $p_s(\tau, f_d)$  is the coherent scattering power of DDM. Surface differentiation  $d^2\rho$  can be expressed as follows.

$$d^2\rho = |J(\tau_{xy}, f_d, xy)| d\tau_{xy} d f_d, xy \quad (29)$$

$$\langle |Y(\tau, f_d)|^2 \rangle = \chi^2(\tau, f_d)$$

$$* \left( T_i^2 \frac{D^2(\vec{\rho}(\tau, f_d)) \sigma_0(\vec{\rho}(\tau, f_d))}{4\pi R_0^2(\vec{\rho}(\tau, f_d)) R^2(\vec{\rho}(\tau, f_d))} |J(\tau, f_d)| \right) \quad (30)$$

$$p_s(\tau, f_d) = \frac{T_i^2}{4\pi} \left( \frac{D^2(\vec{\rho}_1(\tau, f_d)) \cdot \sigma_0(\vec{\rho}_1(\tau, f_d))}{R_0^2(\vec{\rho}_1(\tau, f_d)) \cdot R^2(\vec{\rho}_1(\tau, f_d))} |J_1(\tau, f_d)| \right) + \frac{T_i^2}{4\pi} \left( \frac{D^2(\vec{\rho}_2(\tau, f_d)) \cdot \sigma_0(\vec{\rho}_2(\tau, f_d))}{R_0^2(\vec{\rho}_2(\tau, f_d)) \cdot R^2(\vec{\rho}_2(\tau, f_d))} |J_2(\tau, f_d)| \right) \quad (31)$$

The Fresnel reflection coefficient governs the energy relationship between incident electromagnetic waves and reflections at the interface, accounting for the influence of incident signal angle and the complex dielectric constant of the reflecting surface on GNSS reflection signals. The specific formula for the Fresnel reflection coefficient is as follows.

$$\Re_{VV} = \frac{\varepsilon \sin \theta - \sqrt{\varepsilon - \cos^2 \theta}}{\varepsilon \sin \theta + \sqrt{\varepsilon - \cos^2 \theta}} \quad (32)$$

$$\Re_{HH} = \frac{\sin \theta - \sqrt{\varepsilon - \cos^2 \theta}}{\sin \theta + \sqrt{\varepsilon - \cos^2 \theta}} \quad (33)$$

$$\Re = \Re_{RL} = \frac{1}{2} (\Re_{VV} - \Re_{HH}) \quad (34)$$

In the formula,  $\varepsilon$  represents the complex dielectric constant at sea level.  $R$ ,  $L$ ,  $V$ , and  $H$  denote right-handed circular polarization, left-handed circular polarization, vertical polarization, and horizontal polarization, respectively, while  $\theta$  signifies the satellite altitude angle. Taking GPS signal as an example, if the complex dielectric constant of seawater is  $\varepsilon = 70.53 + 65.68j$ , the correlation characteristics of the GNSS-R signal can be related to the satellite altitude angle in Fig. 11.

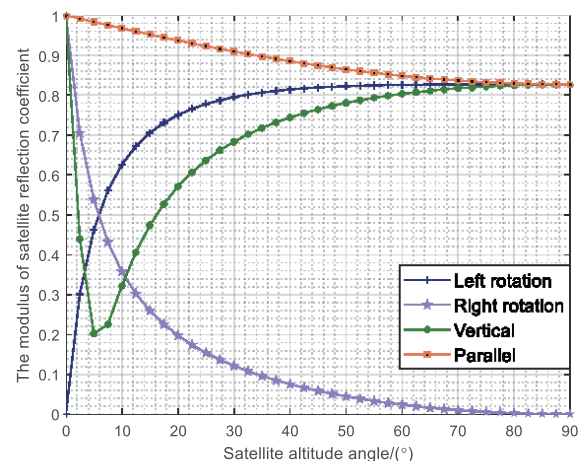


FIGURE 11. The variation of satellite altitude angle with the modulus of reflection coefficient under different polarization conditions.

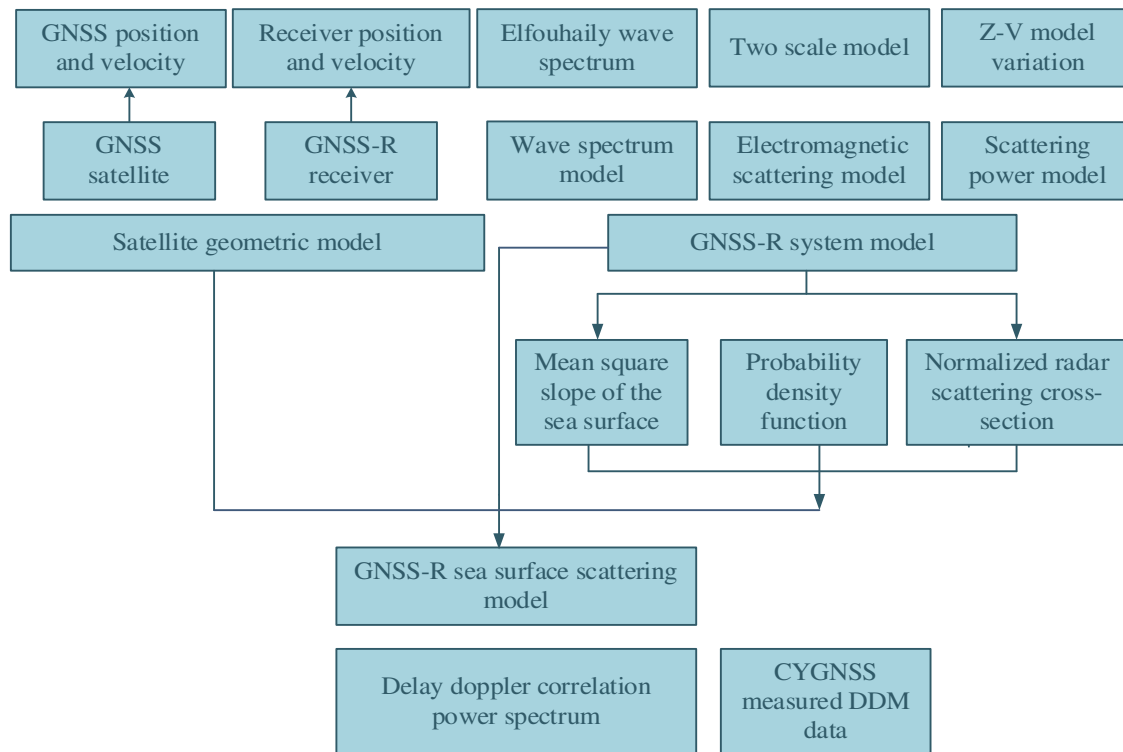


FIGURE 12. Flowchart of DDM simulation.

To receive low grazing angle reflection signals, typically associated with elevation  $6.8^\circ$  angles approximately greater than a certain threshold, position the low-gain right-handed polarization antenna facing upward. This orientation optimizes the reception of direct signals emitted by GPS satellites. A high-gain, left-handed polarized antenna is positioned facing downwards to receive signals reflected from the surface of the sea. When the signal reflects off the sea surface, it predominantly acquires left-handed polarization components, which causes the polarity to undergo rotation, thus facilitating enhanced energy conversion. Furthermore, as shown in Fig. 11, the right-handed and horizontal polarization components gradually decrease with the increase in satellite altitude angle, and the left-handed and vertical polarization components increase. When the elevation angle of a left-handed satellite is less than  $35^\circ$ , the rate of change in the modulus of reflection coefficient is relatively fast. However, when the elevation angle is greater than  $35^\circ$ , the change tends to stabilize.

## 5. RESULTS AND DISCUSSION

### 5.1. DDM Simulation and Analysis

Therefore, it is necessary to integrate various simulation application requirements and establish corresponding parameters. The GNSS-R signal simulation DDM process is illustrated in Fig. 12.

This article chooses the GPS L1 C/A signal as the raw signal for DDM simulation, with a signal frequency of 1.57542 GHz. The heights of the transmitter and receiver are 20200000m

and 630000m, respectively. After coordinate conversion, the position and velocity coordinates of the GPS transmitter are  $(-7009700, 0, 19259000)$  and  $(-3638.9, 0, -1324.5)$ , respectively. The position and speed of the receiver are  $(227950, 0, 626210)$  and  $(7086.5, 0, -2579.3)$ , respectively. Coherent integration time is  $0.001s$ , and the wind speed is  $U_{10} = 3m/s$ . The satellite altitude angle is set to  $\theta = 70^\circ$ . The sea surface inverse wave age is set to  $\Omega = 0.84$ , and a fully developed marine environment is selected. Employ the previously delineated parameters for the forthcoming DDM simulation.

The conventional KA-GO electromagnetic scattering method and two scale electromagnetic scattering method were utilized to acquire distinct WAF functions and DDM images in the simulation process. An example is shown as Fig. 13 and Fig. 14. In scenarios where the imaging area encompasses complete isochronous loops and iso-Doppler bands, the resolution of iso-Doppler lines solely based on Doppler frequency becomes unattainable. When a Doppler loop is segmented using multiple delay lines, regions exhibiting identical delay values will appear. Following the cross-interaction between the spatial and frequency domains, ghosting phenomena arise in the image domain, consequently inducing spatial resolution degradation, a phenomenon similarly observed in delay lines. Therefore, Fig. 13 and Fig. 14 illustrate two different methods of mapping from the delay Doppler domain to the spatial domain. Therefore, blurring position can be observed, which is caused by the two corresponding areas around the specular reflection point on the sea surface.

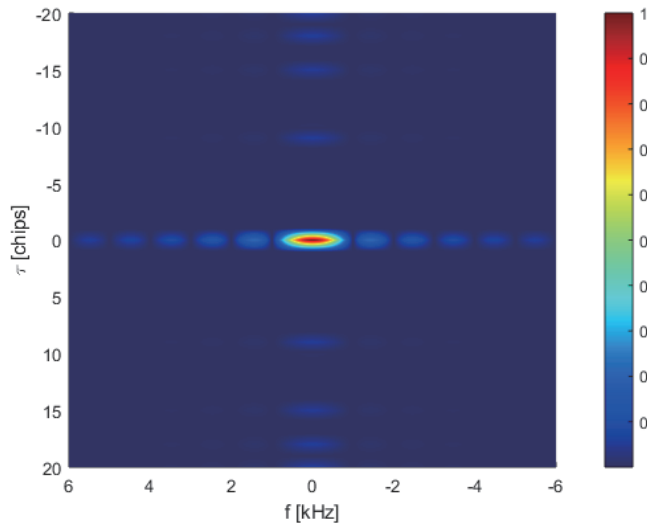


FIGURE 13. WAF function obtained by KA-GO method.

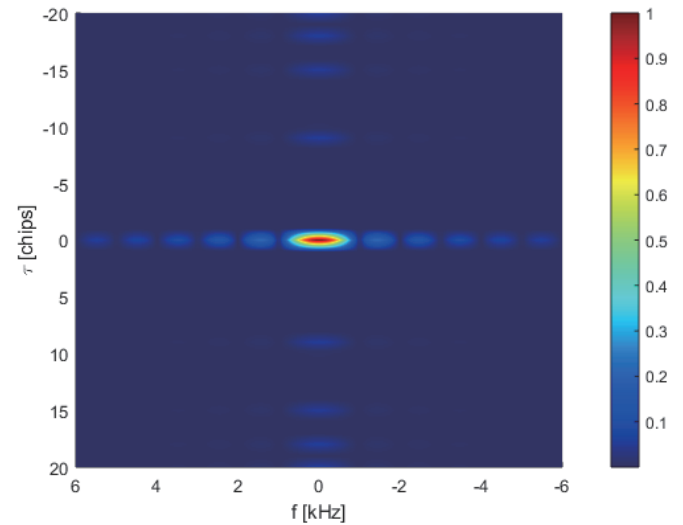


FIGURE 14. WAF function obtained by TSM method.

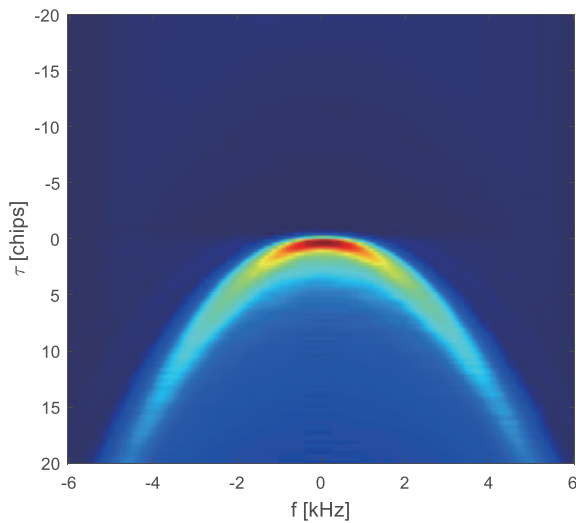


FIGURE 15. DDM obtained by KA-GO method.

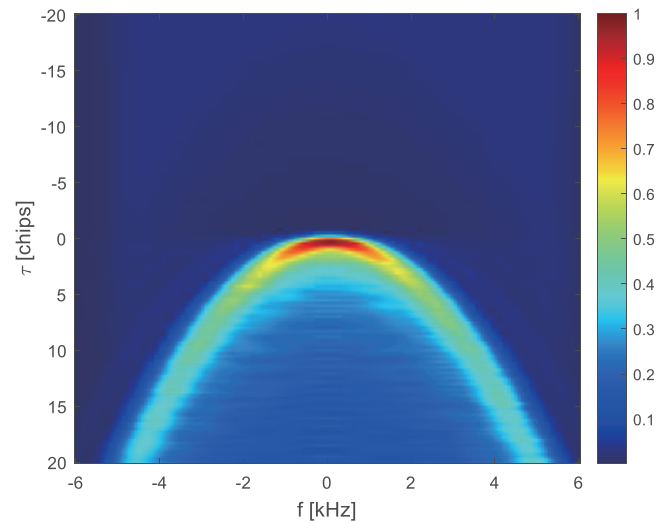


FIGURE 16. DDM obtained by TSM method.

This article calculates the two-dimensional delay Doppler correlation power based on Eq. (30). The DDMs simulated using KA-GO and TSM methods are shown in Fig. 15 and Fig. 16. To facilitate the extraction of the disparity in DDM values between the two methodologies, the disparity between their respective DDMs was computed, with the resultant image depicted in Fig. 17. The example of  $\sigma$  generated on the sea surface is shown in Fig. 18.

In the process of DDM imaging analysis, there are many factors that can affect the peak value of DDM, thereby affecting the retrieval of geophysical parameters and the interpretability of the final data. Due to the relative motion and delay difference between GNSS navigation satellites and receivers, the receivers receive relative Doppler frequency differences between different scattering points on the sea surface. Therefore, in order to explore the impact of different Doppler and delay intervals on DDM, the following assumptions are made for the parameters. Assume that the heights of GNSS satellite and low

orbit satellite receivers are 20200000 m and 630000 m, respectively. The satellite altitude angle is  $70^\circ$ . When a fixed delay interval of 0.25 chips is maintained, the reflection area is partitioned into equidistant delay and equidistant Doppler lines, each with varying Doppler intervals within the same reflection area. Figs. 19(a)–(d) use the same delay interval of 0.25 chips, with Doppler intervals of 80 Hz, 125 Hz, 200 Hz, and 500 Hz, respectively. The simulated DDMs corresponding to different Doppler intervals are shown in Figs. 20(a)–(d).

The Doppler region is a strip, and the scattering area is divided into a single wind zone range by Doppler frequency, which is relatively rough. By determining the range and size of the time delay Doppler interval, the size of the reflection surface unit and the spatial resolution of the observation are determined. At that time, the delay interval was fixed, and the smaller the Doppler interval is, the lower the resolution is. The impact of delay interval on DDM is the same. Different ocean developments can also affect MSS, ultimately affecting imaging. In

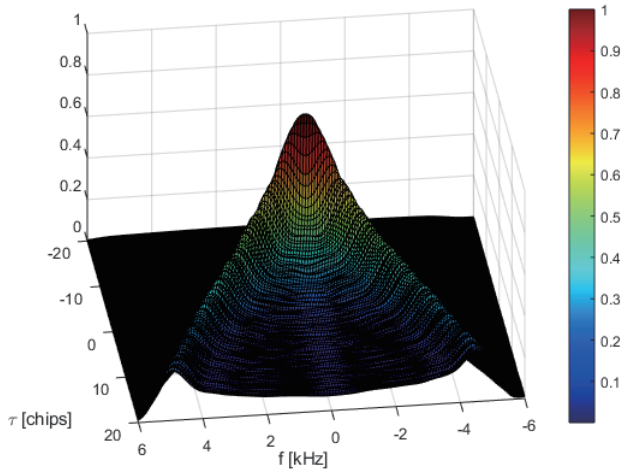


**FIGURE 17.** The difference of DDM between KA-GO method and TSM method.

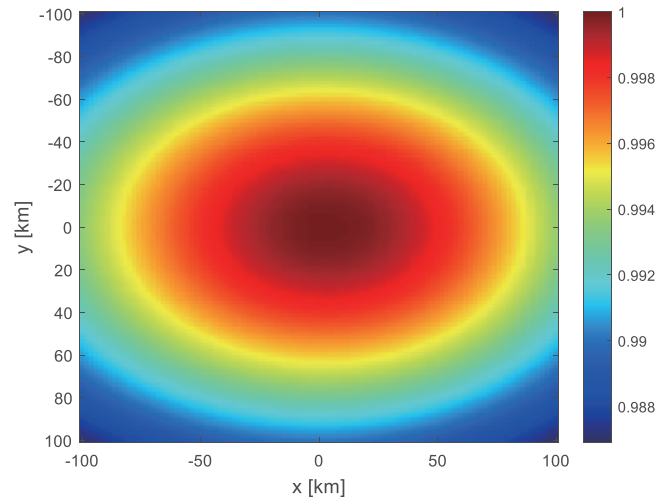


**FIGURE 18.** Example of  $\sigma$  generated on the sea surface.

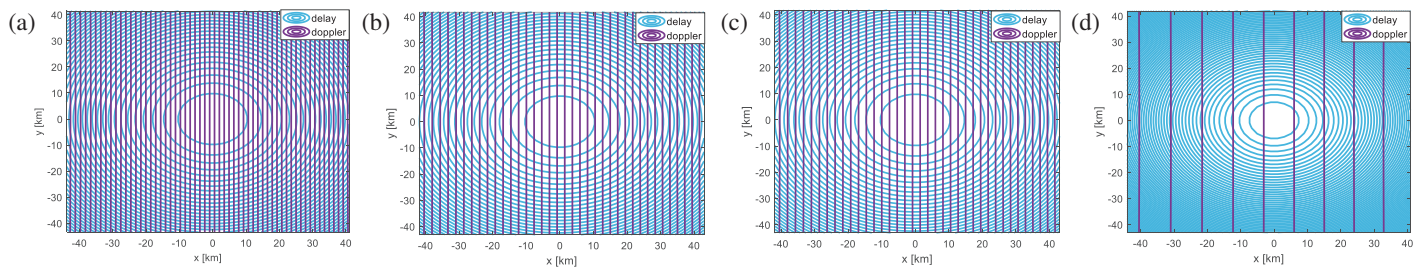


**FIGURE 19.** Iso-delay and iso-Doppler lines with different Doppler interval under fixed delay interval 0.25 chips. (a) Doppler interval is 80 Hz; (b) Doppler interval is 125 Hz; (c) Doppler interval is 200 Hz; (d) Doppler interval is 500 Hz.

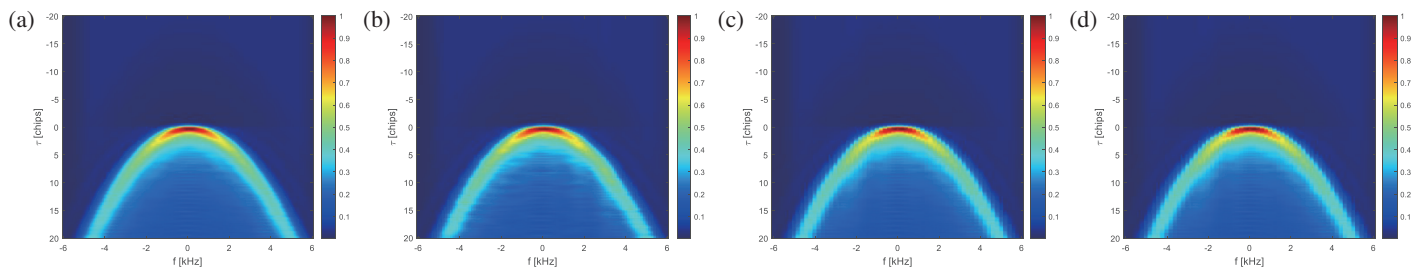


**FIGURE 20.** The simulated DDMs with different Doppler intervals. (a) DDM with delay interval of 0.25 chips and Doppler interval of 80 Hz; (b) DDM with delay interval of 0.25 chips and Doppler interval of 125 Hz; (c) DDM with delay interval of 0.25 chips and Doppler interval of 200 Hz; (d) DDM with delay interval of 0.25 chips and Doppler interval of 500 Hz.

the simulation process, varying degrees of ocean development are selected. The inverse wave age serves as a metric to denote the level of wave development, thereby serving as a pertinent factor in gauging sea conditions. When inverse wave age  $\Omega$  is 0.84, 1, and greater than 2, the corresponding ocean states are fully developed, mature, and young, respectively. The subsequent alterations in MSS values correspond to fluctuations in sea conditions induced by differing inverse wave ages.

As depicted in Fig. 21(a), it is evident that with the progressive escalation of wind speed, MSS exhibits a continuous augmentation. This phenomenon arises due to the absence of fully formed long waves. Consequently, matured sea conditions exhibit a larger MSS than younger oceans. As depicted in

Fig. 21(b), as the elevation angle of the satellite decreases, the peak value of DDM decreases with the wind speed.

### 5.2. Comparison of DDM with Measured CYGNSS Data

Select the L1 level 2.1 of CYGNSS FM06 satellite corresponding to September 16, 2023, as well as the corresponding raw intermediate frequency data for analysis. The unprocessed raw intermediate frequency data can be processed to obtain processed DDM and one-dimensional delay waveforms as shown in Fig. 22. A one-dimensional delay waveform is a delay waveform obtained by cutting along the DDM peak at a constant Doppler frequency.

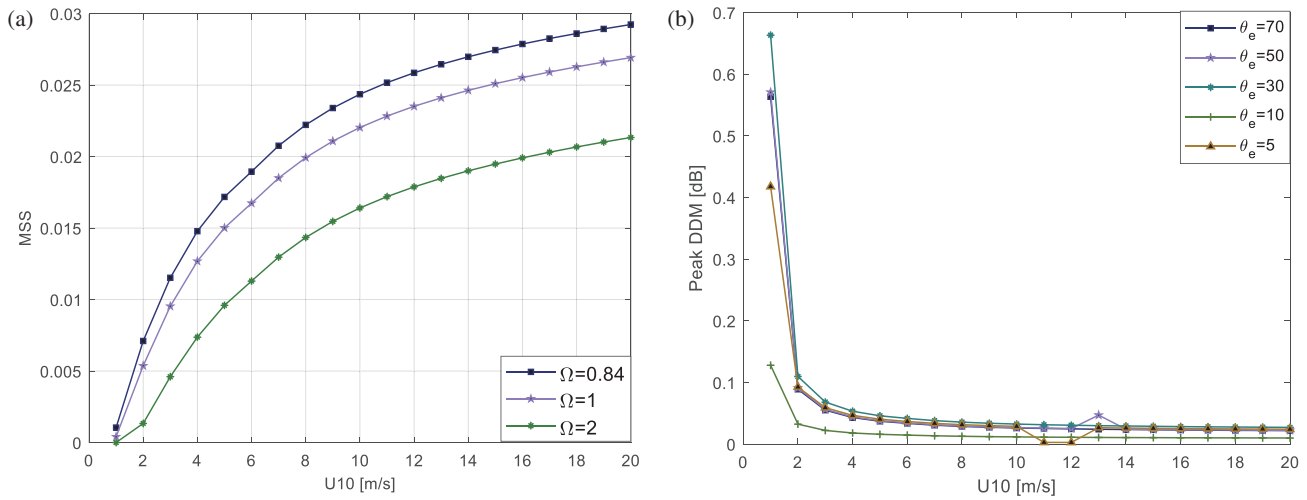


**FIGURE 21.** The variation of MSS with wind speed under different conditions. (a) The variation of MSS with wind speed under different inverse wave age; (b) The variation of MSS with wind speed under different elevation angles.

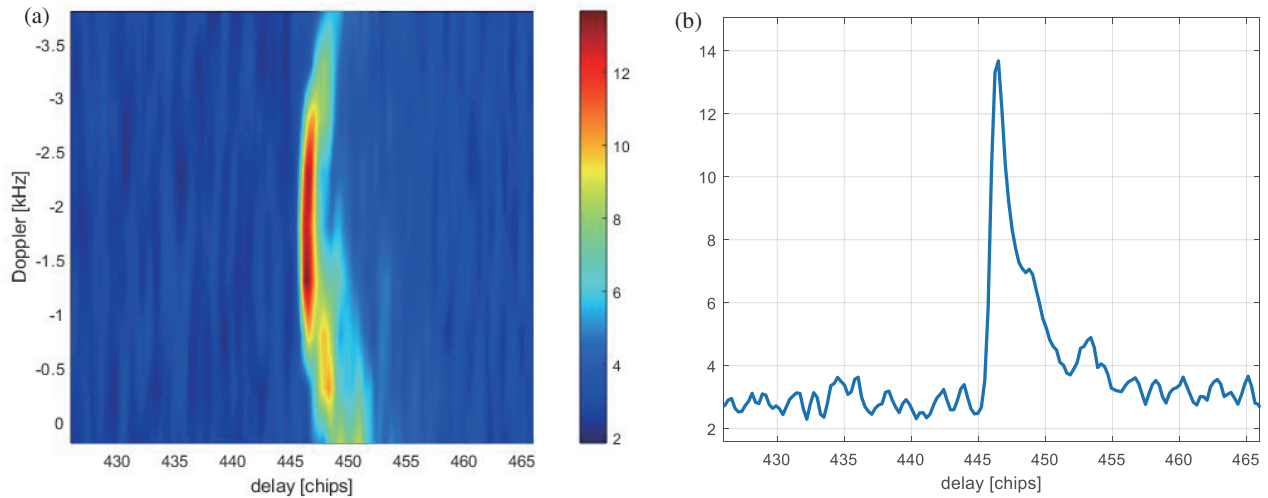


**FIGURE 22.** DDM and WF obtained by processing CYGNSS raw intermediate frequency data. (a) DDM from the L1 level 2.1 of CYGNSS; (b) WF from the L1 level 2.1 of CYGNSS.

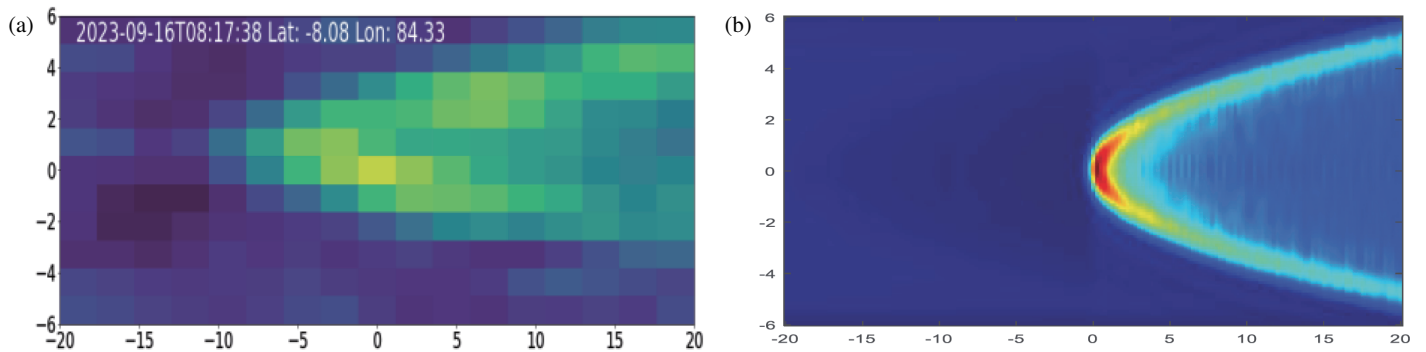


**FIGURE 23.** Comparison of measured and simulated DDMs. (a) Measured DDM. (b) Simulated DDM.

This article reads the data from the CYGNSS04 satellite on September 16, 2023. The CYGNSS DDM reflection processing uses the first reflection channel. Fig. 23 shows the DDM

obtained through the processing of the measured data from the CYGNSS satellite. The comparison and analysis between the measured data from the CYGNSS satellite and the simulated

results of the two-dimensional delay Doppler power spectrum obtained under the same simulation scenario are presented.

Fig. 23 illustrates that the DDM waveforms derived from CYGNSS measured data processing closely align with those obtained from simulation. The reflection intensity of the reflected signal demonstrates uniformity across various reflection surface units, indicating consistent characteristics throughout. The signal related power received by the CYGNSS constellation and the simulated signal exhibit a classic “horseshoe shaped” distribution in the delay Doppler domain. At that time, the delay gradually increased, corresponding to the appearance of larger iso-delay ellipses. When the iso-delay ellipse is used for iso-Doppler band cutting, the maximum set of both occurs at the two Doppler frequencies of the ellipse cutting. The distance between the mirror reflection frequency and the two nearby tangential Doppler frequencies continues to increase. Therefore, the DDM simulation image appears horseshoe shaped. The color gradient of the DDM reveals that the scattered signal proximal to the scintillation zone exhibits heightened intensity, whereas signals distant from the scintillation zone display diminished reflection intensity. Furthermore, these distant signals exert a relatively minor influence on the overall signal power.

## 6. CONCLUSION

By virtue of a modified Z-V model combined with TSM for sea surface scattering, this paper focuses on the modeling and analysis of delay Doppler maps for spaceborne GNSS-R signal from sea surface, with emphasis on the influence of wind speed, inverse wave age, delay Doppler interval on DDM signature. Numerical simulations indicate that the peak value of DDM is significantly affected by sea states, because the value of MSS increases with wind speed increasing under different elevation angles and inverse wave age conditions. It is also demonstrated that the reliability of DDM simulation waveforms is affected by delay interval as well as Doppler interval, and a smaller delay-Doppler interval gives rise to a good match between the simulated DDM waveform and theoretical waveform. The DDM of GNSS scattering signal from sea surface is validated by comparison with measured CYGNSS DDM data in L1 level 2.1 version, thus verifying the effectivity of the modeling method in this paper. It deserves further exploration to analyze the effects of power calibration deviation, specular reflection point position error, and other factors. The DDM modeling method in this paper is applicable to satellites currently in orbit, such as CYGNSS, TDS-1, and BuFeng-1 AB satellite. In future study, more accurate electromagnetic scattering model will be developed for the analysis in complex scenarios, such as sea surface with sea ice, sea under high sea state, sea surface with oil spill, and sea with wave breaking.

## ACKNOWLEDGEMENTS

This work was supported in part by the National Natural Science Foundation of China [Grant Nos. 62061048, 62461054, 62261054, and 62361054], in part by the Shaanxi Key Research and Development Program [Grant Nos. 2023-YBGY-254, and

2024GXBYXM-108], in part by the Yan’an Science and Technology Plan Project [2023-GYGG-024], in part by the Natural Science Basic Research Plan in Shaanxi Province of China (Grant No. 2023-JC-YB-539), and in part by Yulin City Project of Industry-Academia-Research Cooperation (Grant No. CXY-2022-188).

## REFERENCES

- [1] Rodriguez-Alvarez, N., J. F. Munoz-Martin, and M. Morris, “Latest advances in the global navigation satellite system-reflectometry (GNSS-R) field,” *Remote Sensing*, Vol. 15, No. 8, 2157, 2023.
- [2] Kuschel, H., D. Cristallini, and K. E. Olsen, “Tutorial: Passive radar tutorial,” *IEEE Aerospace and Electronic Systems Magazine*, Vol. 34, No. 2, 2–19, 2019.
- [3] Hofmann-Wellenhof, B., H. Lichtenegger, and E. Wasle, *GNSS-Global Navigation Satellite Systems: GPS, GLONASS, Galileo, and More*, Springer Science & Business Media, 2007.
- [4] Carreno-Luengo, H., A. Camps, C. Ruf, N. Floury, M. Martin-Neira, T. Wang, S. J. Khalsa, M. P. Clarizia, J. Reynolds, J. Johnson, *et al.*, “The IEEE-SA working group on spaceborne GNSS-R: Scene study,” *IEEE Access*, Vol. 9, 89 906–89 933, 2021.
- [5] Hu, Y., Z. Jiang, W. Liu, X. Yuan, Q. Hu, and J. Wickert, “GNSS-R sea ice detection based on linear discriminant analysis,” *IEEE Transactions on Geoscience and Remote Sensing*, Vol. 61, 1–12, 2023.
- [6] Hu, Y., X. Hua, W. Liu, and J. Wickert, “Sea ice detection from GNSS-R data based on residual network,” *Remote Sensing*, Vol. 15, No. 18, 4477, 2023.
- [7] Kim, S., J. L. Garrison, and M. Kurum, “Retrieval of subsurface soil moisture and vegetation water content from multifrequency soop reflectometry: Sensitivity analysis,” *IEEE Transactions on Geoscience and Remote Sensing*, Vol. 61, 1–18, 2023.
- [8] Yang, C., K. Mao, Z. Guo, J. Shi, S. M. Bateni, and Z. Yuan, “Review of GNSS-R technology for soil moisture inversion,” *Remote Sensing*, Vol. 16, No. 7, 1193, 2024.
- [9] Ding, Q., Y. Liang, X. Liang, C. Ren, H. Yan, Y. Liu, Y. Zhang, X. Lu, J. Lai, and X. Hu, “Soil moisture retrieval using GNSS-IR based on empirical modal decomposition and cross-correlation satellite selection,” *Remote Sensing*, Vol. 15, No. 13, 3218, 2023.
- [10] Issa, H., G. Stienne, S. Reboul, M. Raad, and G. Faour, “High-rate GNSS reflectometry for water body detection using low altitude airborne carrier,” in *2021 IEEE Specialist Meeting on Reflectometry using GNSS and other Signals of Opportunity (GNSS+R)*, 9–12, Beijing, China, Sep. 2021.
- [11] Chen, F., L. Liu, F. Guo, and L. Huang, “A new vegetation observable derived from spaceborne GNSS-R and its application to vegetation water content retrieval,” *Remote Sensing*, Vol. 16, No. 5, 931, 2024.
- [12] Clarizia, M. P., C. P. Gommenginger, S. T. Gleason, M. A. Srokosz, C. Galdi, and M. D. Bisceglie, “Analysis of GNSS-R delay-Doppler maps from the UK-DMC satellite over the ocean,” *Geophysical Research Letters*, Vol. 36, No. 2, 2009.
- [13] Wang, F., D. Yang, W. Li, and W. Yang, “On-ground retracking to correct distorted waveform in spaceborne global navigation satellite system-reflectometry,” *Remote Sensing*, Vol. 9, No. 7, 643, 2017.
- [14] Clarizia, M. P., C. Gommenginger, S. Gleason, C. Galdi, and M. Unwin, “Global navigation satellite system-reflectometry (GNSS-R) from the UK-DMC satellite for remote sensing of the ocean surface,” in *IGARSS 2008 — 2008 IEEE Interna-*

- tional Geoscience and Remote Sensing Symposium*, Vol. 1, 1–276, Boston, MA, USA, Jul. 2008.
- [15] Foti, G., C. Gommenginger, P. Jales, M. Unwin, A. Shaw, C. Robertson, and J. Roselló, “Spaceborne GNSS reflectometry for ocean winds: First results from the UK TechDemoSat-1 mission,” *Geophysical Research Letters*, Vol. 42, No. 13, 5435–5441, 2015.
- [16] Rius, A., E. Cardellach, F. Fabra, W. Li, S. Ribó, and M. Hernández-Pajares, “Feasibility of GNSS-R ice sheet altimetry in Greenland using TDS-1,” *Remote Sensing*, Vol. 9, No. 7, 742, 2017.
- [17] Wickert, J., G. Beyerle, E. Cardellach, C. Förste, T. Gruber, A. Helm, M. P. Hess, P. Høeg, N. Jakowski, O. Montenbruck, et al., “GNSS reflectometry, radio occultation and scatterometry onboard ISS for long-term monitoring of climate observations using innovative space geodetic techniques on-board the international space station,” *Proposal in Response to Call: ESA Research Announcement for ISS Experiments relevant to study of Global Climate Change*, 2011.
- [18] Ribó, S., J. C. Arco-Fernández, E. Cardellach, F. Fabra, W. Li, O. Nogués-Correig, A. Rius, and M. Martín-Neira, “A software-defined GNSS reflectometry recording receiver with wide-bandwidth, multi-band capability and digital beam-forming,” *Remote Sensing*, Vol. 9, No. 5, 450, 2017.
- [19] Ruf, C., M. Unwin, J. Dickinson, R. Rose, D. Rose, M. Vincent, and A. Lyons, “CYGNSS: Enabling the future of hurricane prediction [remote sensing satellites],” *IEEE Geoscience and Remote Sensing Magazine*, Vol. 1, No. 2, 52–67, 2013.
- [20] Hou, Z. and Z. Pu, “Assessing CYGNSS satellite soil moisture data for drought monitoring with multiple datasets and indicators,” *Remote Sensing*, Vol. 16, No. 1, 116, 2023.
- [21] Liu, Q., S. Zhang, W. Li, Y. Nan, J. Peng, Z. Ma, and X. Zhou, “Using robust regression to retrieve soil moisture from CyGNSS data,” *Remote Sensing*, Vol. 15, No. 14, 3669, 2023.
- [22] Yu, K., S. Han, J. Bu, Y. An, Z. Zhou, C. Wang, S. Tabibi, and J. W. Cheong, “Spaceborne GNSS reflectometry,” *Remote Sensing*, Vol. 14, No. 7, 1605, 2022.
- [23] Blackwell, W. J., “NASA tropics pathfinder and constellation mission preparations for launches in 2021 and 2022,” in *2021 IEEE International Geoscience and Remote Sensing Symposium IGARSS*, 1511–1513, Brussels, Belgium, Jul. 2021.
- [24] Jing, C., X. Niu, C. Duan, F. Lu, G. Di, and X. Yang, “Sea surface wind speed retrieval from the first Chinese GNSS-R mission: Technique and preliminary results,” *Remote Sensing*, Vol. 11, No. 24, 3013, 2019.
- [25] Zhang, Y., Z. Yan, S. Yang, W. Meng, S. Gu, J. Qin, Y. Han, and Z. Hong, “Research on shore-based river flow velocity inversion model using GNSS-R raw data,” *Remote Sensing*, Vol. 14, No. 5, 1170, 2022.
- [26] Garrison, J. L., S. J. Katzberg, V. U. Zavorotny, and D. Masters, “Comparison of sea surface wind speed estimates from reflected GPS signals with buoy measurements,” in *IGARSS 2000. IEEE 2000 International Geoscience and Remote Sensing Symposium. Taking the Pulse of the Planet: The Role of Remote Sensing in Managing the Environment. Proceedings (Cat. No.00CH37120)*, Vol. 7, 3087–3089, Honolulu, HI, USA, Jul. 2000.
- [27] Garrison, J. L., A. Komjathy, V. U. Zavorotny, and S. J. Katzberg, “Wind speed measurement using forward scattered GPS signals,” *IEEE Transactions on Geoscience and Remote Sensing*, Vol. 40, No. 1, 50–65, 2002.
- [28] Bu, J., K. Yu, H. Park, W. Huang, S. Han, Q. Yan, N. Qian, and Y. Lin, “Estimation of swell height using spaceborne GNSS-R data from eight CYGNSS satellites,” *Remote Sensing*, Vol. 14, No. 18, 4634, 2022.
- [29] O’Brien, A. and J. T. Johnson, “Comparing the CYGNSS simulator forward scattering model with TDS-1 and CYGNSS on-orbit DDMS,” in *2017 IEEE International Geoscience and Remote Sensing Symposium (IGARSS)*, 2657–2658, Fort Worth, TX, USA, Jul. 2017.
- [30] Bai, W., J. Xia, D. Zhao, Y. Sun, X. Meng, C. Liu, Q. Du, X. Wang, D. Wang, D. Wu, C. Wu, C. Liu, and Y. Cai, “GREEPS: An GNSS-R end-to-end performance simulator,” in *2016 IEEE International Geoscience and Remote Sensing Symposium (IGARSS)*, 4831–4834, Beijing, China, Jul. 2016.
- [31] Pierdicca, N., L. Guerriero, R. Giusto, M. Brogioni, and A. Egido, “SAVERS: A simulator of GNSS reflections from bare and vegetated soils,” *IEEE Transactions on Geoscience and Remote Sensing*, Vol. 52, No. 10, 6542–6554, 2014.
- [32] Melebari, A., J. D. Campbell, E. Hodges, and M. Moghaddam, “Improved geometric optics with topography (IGOT) model for GNSS-R delay-doppler maps using three-scale surface roughness,” *Remote Sensing*, Vol. 15, No. 7, 1880, 2023.
- [33] Nabi, M. M., V. Senyurek, A. C. Gurbuz, and M. Kurum, “A deep learning-based soil moisture estimation in conus region using cygnss delay doppler maps,” in *IGARSS 2022-2022 IEEE International Geoscience and Remote Sensing Symposium*, 6177–6180, Kuala Lumpur, Malaysia, Jul. 2022.
- [34] Carreno-Luengo, H., C. S. Ruf, S. Gleason, and A. Russel, “An improved inland water detector using standard L1 data: Application to CYGNSS,” in *IGARSS 2023-2023 IEEE International Geoscience and Remote Sensing Symposium*, 4322–4323, Pasadena, CA, USA, Jul. 2023.
- [35] Clarizia, M. P. and C. S. Ruf, “Statistical derivation of wind speeds from CYGNSS data,” *IEEE Transactions on Geoscience and Remote Sensing*, Vol. 58, No. 6, 3955–3964, 2020.
- [36] Saïd, F., Z. Jelenak, J. Park, and P. S. Chang, “The noaa track-wise wind retrieval algorithm and product assessment for cygnss,” *IEEE Transactions on Geoscience and Remote Sensing*, Vol. 60, 1–24, 2021.
- [37] Li, C. and W. Huang, “Simulating GNSS-R delay-doppler map of oil slicked sea surfaces under general scenarios,” *Progress In Electromagnetics Research B*, Vol. 48, 61–76, 2013.
- [38] Gu, W., H. Xu, and L. Tsang, “A numerical Kirchhoff simulator for GNSS-R land applications,” *Progress In Electromagnetics Research*, Vol. 164, 119–133, 2019.
- [39] Zavorotny, V. U. and A. G. Voronovich, “Scattering of GPS signals from the ocean with wind remote sensing application,” *IEEE Transactions on Geoscience and Remote Sensing*, Vol. 38, No. 2, 951–964, 2000.